Journal of Alloys and Compounds 505 (2010) 762–767

Contents lists available at ScienceDirect

Journal of Alloys and Compounds

journal homepage: www.elsevier.com/locate/jallcom

Structural instability and photoacoustic study of AlSb prepared by mechanical alloying

D.M. Trichês [a], S.M. Souza [a], C.M. Poffo [a], J.C. de Lima [b,*], T.A. Grandi [b], R.S. de Biasi [c]

[a] Departamento de Engenharia Mecânica, Universidade Federal de Santa Catarina, 88040-900 Florianópolis, SC, Brazil
[b] Departamento de Física, Universidade Federal de Santa Catarina, 88040-900 Florianópolis, SC, Brazil
[c] Seção de Engenharia Mecânica e de Materiais, Instituto Militar de Engenharia, 22290-270 Rio de Janeiro, RJ, Brazil

ARTICLE INFO

Article history:
Received 3 March 2010
Received in revised form 21 June 2010
Accepted 23 June 2010
Available online 1 July 2010

PACS:
61.05.cp
64.70.kg
66.30.Xj
66.10.cd

Keywords:
Semiconductor
Thermal diffusivity
X-ray diffraction
Photoacoustic absorption
Mechanical alloying

ABSTRACT

High-purity elemental Al and Sb powders were blended with equiatomic composition and submitted to mechanical alloying. For all milling times, the milled powders showed a mixture of AlSb and elemental Sb. The largest amount of AlSb was reached for milling times between 7 and 10 h. For milling times larger than 10 h, decomposition of AlSb was observed. The volume fractions of the crystalline and interfacial components were estimated using the X-ray diffraction pattern of a sample milled for 10 h. Photoacoustic absorption spectroscopy (PAS) was used to determine the thermal diffusivity and other heat transport parameters in the same sample. A combination of XRD and PAS data was used to estimate the thermal diffusivity of the interfacial component, which has a significant contribution to the thermal diffusivity of the sample.

© 2010 Elsevier B.V. All rights reserved.

1. Introduction

Aluminum antimonide (AlSb) is a semiconductor of considerable importance. Potentially it can be highly resistive and is closely lattice matched to GaSb and therefore has been used as semi-insulating substrate or buffer layer for the epitaxial growth of GaSb [1,2]. AlSb has an indirect band gap with an energy of 1.62 eV [3] and thus is a good candidate for applications such as high-energy photon detectors and as a barrier material to confine electrons in antimonide heterostructure devices [4], in InAs-channel high electron mobility transistors [5,6] and magnetoelectronic hybrid Hall effect devices [7].

AlSb can be produced using several techniques [8–10], including mechanical alloying (MA). MA is an efficient technique to synthesize many unique materials such as nanostructured alloys, amorphous alloys, and metastable solid solutions [11–13]. It has also been used to produce commercially important alloys whose components have a high melting point [14]. MA has many advantages, including processing at low temperatures, easy composition control, inexpensive equipment, and the possibility of scaling up. Its disadvantage is contamination by the milling media and possibly by the milling atmosphere.

Nanostructured materials are metastable and have two components: crystallites with nanometer dimensions, <100 nm, which have same characteristics as the bulk crystal, and an interfacial phase formed by different kinds of defects (grain boundaries, interphase boundaries, dislocations, etc.) [15]. The number of atoms is similar in both components, making the properties of the nanostructured materials to dependent on the atomic arrangements of the interfacial component. From the technological point of view, manipulation of the interfacial component offers the possibility of designing new materials with physical properties for specific applications [15,16].

The Al–Sb phase diagram [17] exhibits only the equiatomic AlSb compound, which has a cubic structure. Honda et al. [18] prepared AlSb by MA using a high-energy planetary ball mill (Itoh, LP-4/2) at 300 rpm and at room temperature. The compound was formed after 5 h of milling and no changes on the measured X-ray diffraction (XRD) patterns were observed for milling times up to 60 h. In another study, Park and Sohn [19] produced mechanically alloyed AlSb powder using a HEMM vibratory mill for 24 h.

* Corresponding author. Tel.: +55 48 3331 6832; fax: +55 48 3331 9758.
E-mail address: fsc1jcd@fsc.ufsc.br (J.C. de Lima).

0925-8388/$ – see front matter © 2010 Elsevier B.V. All rights reserved.
doi:10.1016/j.jallcom.2010.06.137

Due to the technological importance of the Al–Sb system and nanostructured materials, we focused our research on producing AlSb in nanometric form by MA. Since the MA technique yields materials containing a high concentration of defects, we investigated the influence of these defects on the thermal diffusivity measured by photoacoustic absorption spectroscopy (PAS). This paper reports the results of XRD and PAS measurements on AlSb produced by MA.

2. Theoretical background

Thermal diffusivity is defined as $\alpha = k/\rho c$, where k is the thermal conductivity, ρ the mass density and c the specific heat. It is an important physical parameter due not only to its intrinsic physical interest but also to its use in the modeling and designing of technological devices based on semiconductor materials. Physically, the inverse of α is a measure of the time required to establish thermal equilibrium in a given material. As in the case of the optical absorption coefficient, its value is different for each material. Furthermore, the thermal diffusivity is known to be strongly dependent on the effects of compositional and microstructural variables [20], as well as processing conditions [21]. Thus, an appropriate strategy to monitor the structural changes in mixtures submitted to the MA process is to measure the α parameter.

When a modulated light beam impinges on the material inside a photoacoustic gas cell, the absorbed light is converted into periodic heat and a PAS signal is created. The dependence of the PAS signal on the optical absorption coefficient and the light-to-heat conversion efficiency may be used to determine the nonradiative de-excitation efficiency, the photoinduced energy conversion, etc. The PAS signal is directly proportional to the light-to-heat conversion efficiency due to nonradiative processes in the material [20]. For a thermally thick semiconductor sample, there are four processes that may contribute to the PAS signal:

(1) Intraband nonradiative thermalization (thermal diffusion): when the absorbed photon energy is greater than the band gap, an electron is created in the conduction band and a hole is left in the valence band. The excess energies of the electron (the energy difference between the lower edge of the conduction band and the initial energy of the photogenerated electron) and hole (the energy difference between the upper edge of the valence band and the initial energy of the photogenerated hole) appear in the respective carriers as kinetic energy. The initial electron and hole distributions are not Boltzmann-like, and the first step toward establishing equilibrium is for the electrons and holes to interact among themselves, through carrier-carrier collisions and intervalley scattering, to establish separate Boltzmann distributions of electrons and holes. The Boltzmann distributions of electrons and holes can then be separately assigned electron and hole temperatures that reflect the distributions of kinetic energy in the respective charge carrier populations. If photon absorption produces electrons and holes, each with initial excess kinetic energy at least kT above the conduction and valence bands, both initial carrier temperatures are always above the lattice temperature; these carriers are called hot carriers (i.e., hot electrons and hot holes). This first stage of relaxation or equilibration occurs very rapidly (<100 fs), and this process is often referred to as carrier thermalization (i.e., establishment of a thermal distribution described by Boltzmann statistics). The next step of equilibration is for the hot electrons and hot holes to reach equilibrium with the lattice. The initial lattice temperature is the room temperature, which is lower than the initial hot-electron and hot-hole temperatures. Equilibrium of the hot carriers with the lattice is achieved through carrier–phonon interactions (phonon emission through electron and hole scattering), in which the excess kinetic energy of the carriers is transferred to phonons. Phonon emission results in cooling of the carriers and heating of the lattice until the carrier and lattice temperatures become equal. This process is called carrier cooling [22]. González de la Cruz and Gurevich [23,24] reported the calculation of electron and phonon temperature distribution functions in semiconductors and they also carried out a deeper analysis of these temperature distribution functions in PAS measurements.The contribution of this process to the PAS signal decreases exponentially with the modulation frequency according to the equation

$$S = \frac{A}{f}\exp(-a\sqrt{f}) \tag{1}$$

where $a = l_s\sqrt{\pi/\alpha}$, f is the modulation frequency, l_s is the sample thickness, and α its thermal diffusivity. The PAS signal phase shows a modulation frequency dependence of the type

$$\Phi_{ph} = \frac{\pi}{2} - a\sqrt{f} \tag{2}$$

when this process is present, it occurs in the low frequency range;

(2) Nonradiative bulk recombination: a complete relaxation of the system is reached after electron and hole recombine, either radiatively or nonradiatively. When nonradiative recombination of excess electron–hole pairs occurs after diffusion, it takes place over a distance $\sqrt{D\tau}$. The contribution of this process to the PAS signal shows a modulation frequency dependence of the type $f^{-1.5}$. The thermal diffusivity α, carrier diffusion coefficient D, surface recombination velocity v, and recombination time τ can be determined by fitting the PAS signal phase to the expression given by Pinto Neto et al. [25],

$$\Phi_{ph} = \frac{\pi}{2} + \tan^{-1}\left[\frac{(bD/v)(\omega\tau_{eff}+1)}{(bD/v)(1-\omega\tau_{eff}) - 1 - (\omega\tau_{eff})^2}\right], \tag{3}$$

where $\tau_{eff} = \tau(D/\alpha_s - 1)$, $b = \sqrt{\pi f/\alpha}$, and $\omega = 2\pi f$. When present, this process occurs in the high frequency range after intraband nonradiative thermalizations;

(3) Nonradiative surface recombination: when nonradiative surface recombination of excess electron–hole pairs occurs, it takes place at the sample surface. The contribution of this process to the PAS signal shows a modulation frequency dependence of the type $f^{-1.0}$. Similarly to process (2), the α, D, v, and τ parameters can be determined by fitting the PAS signal phase to the expression given by Pinto Neto et al. [25]. When present, this process occurs in the high frequency range after the nonradiative bulk recombination process; and

(4) Thermoelastic bending: when a temperature gradient is generated within the sample, across its thickness, the thermoelastic bending process contributes to the PAS signal. This contribution shows a modulation frequency dependence of the type $f^{-1.0}$. The thermal diffusivity α can be determined by fitting the PAS signal phase to the expression

$$\Phi_{ph} = \phi_0 + \tan^{-1}\left[\frac{1}{a\sqrt{f}-1}\right], \tag{4}$$

where the constant a is the same defined for process (1). The PAS signal for processes (3) and (4) shows the same dependence on the modulation frequency. However, the PAS signal phase for each process has a different dependence on the modulation frequency. Thus, analysis of the PAS signal phase can be used to distinguish these processes and determine the thermal diffusivity α. When present, this process occurs in the high frequency range after the nonradiative surface recombination process.In

practice, the contribution of each process to the pressure variation in the photoacoustic cell can easily be found through the following procedure: (i) in plots of $\ln S$ versus $\sqrt{f}$ and Φ_{ph} (in radians) versus $\sqrt{f}$, a is the slope of the straight line fitting the data in the low modulation frequency range and the values calculated from both plots must be equal; (ii) in a plot of $\log S$ versus $\log f$, the slope of the straight line fitting the data in the high modulation frequency range highlights the contribution of nonradiative bulk recombination and nonradiative surface recombination. In this case, the α, D, ν and τ parameters are obtained by fitting the plot Φ_{ph} (in radians) versus f, in the appropriate modulation frequency range, to Eq. (3), and (iii) a similar analysis of that described in (ii) is performed to find the contribution of thermoelastic bending. The α parameter is obtained by fitting the plot Φ_{ph} (in radians) versus f, in the appropriate modulation frequency range, to the Eq. (4). This procedure can be executed using the Origin software [26].

3. Experimental procedure

Two equiatomic batches of elemental aluminum (Alfa Aesar, 99.999%) and antimony (Alfa Aesar, 99.999%) powders were prepared. They were sealed together with several steel balls with average diameter 11.5×10^{-3} m in a cylindrical steel container under argon atmosphere. The ball-to-powder weight ratio was 5:1. The vial was mounted on a SPEX mixer/mill model 8000 and the milling was performed at room temperature. A cooling system was used to keep the container temperature close to room temperature. Structural changes with milling times were followed by recording XRD patterns, using a Miniflex Rigaku powder diffractometer, equipped with CuKα radiation (λ = 0.15418 nm). The first batch was milled for 10 and 17 h. The XRD pattern of as-milled powder was well indexed to AlSb and elemental Sb. A decrease of AlSb phase and increase of Sb with milling time was observed. In order to confirm this result, a second batch was milled for 1, 2, 3, 4, 5, 7, 16, 26 and 36 h. The results were similar.

The PAS measurements were performed on a homebuilt open photoacoustic cell (OPC) that includes a 250 W quartz-tungsten-halogen lamp and a Bentham 605 current power supply. After being heat filtered by a water lens, the light is mechanically chopped by a PerkinElmer chopper (model 197) and focused onto the sample. The sample is mounted directly onto the front sound inlet of an electret microphone [27]. The output voltage from the microphone is connected to a computer through a lock-in amplifier in order to record the amplitude and phase of the PAS signal as functions of the modulation frequency. The samples for PAS measurements were prepared by compressing the powder at the same pressure (6 tons or ≈749 MPa) to form tiny circular pellets of 10^{-2} m in diameter. The as-milled sample has thickness of 450 μm. The PAS measurement was taken in the modulation frequency range of 10–270 Hz in order to achieve the thermally thick regime.

4. Results and discussion

4.1. XRD measurements

Fig. 1 shows representative XRD patterns of AlSb for several milling times. The XRD patterns were compared with those given in the ICSD database [28] for the Al–Sb system and with those of elemental Al and Sb. Up to 7 h of milling, the patterns are well indexed to the patterns of cubic AlSb (ICSD code No. 44325) and elemental Sb (ICSD code No. 9859) phases. For 10 h of milling, the XRD pattern is well indexed to cubic AlSb with a small contribution of elemental Sb. For larger milling times, the XRD patterns are well indexed to elemental Sb phase with a small contribution of cubic AlSb. It is interesting to note that elemental Al diffraction lines are not present in the XRD patterns, indicating that a solid solution of Al atoms in the Sb lattice could also be present.

It is interesting to try to understand the partial dissociation of the cubic AlSb phase for milling times larger than 10 h. The ZnS structure is the prototype structure for AlSb, InSb and GaSb. In previous studies, we produced InSb and GaSb by MA and no dissociation of these phases was observed for milling times up 10 h [29,30]. Thus, a comparison with these compounds may be helpful. The TAPP software [17] gives the following values for the enthalpy of formation, lattice parameter and density: $-179.949\ \mathrm{kJ\,mol^{-1}}$, $a = 0.60959$ nm and $5612\ \mathrm{kg/m^3}$ for GaSb; $-69.723\ \mathrm{kJ\,mol^{-1}}$, $a = 0.61355$ nm and $4276\ \mathrm{kg/m^3}$ for AlSb; and $-56.201\ \mathrm{kJ\,mol^{-1}}$, $a = 0.64791$ nm and $5775\ \mathrm{kg/m^3}$ for InSb. The AlSb compound has the smallest density, indicating that it has the least stable structure. For milling times larger than 10 h, a high concentration of defects and strains is introduced into the lattice, causing lattice expansion and, consequently, increasing the internal energy. The combination of these factors may promote the dissociation of AlSb. In another paper [31], we suggested an approach to estimate the volume fractions of the crystalline and interfacial components in nanostructured materials that consists in estimating the contribution of nanometric crystallites to the XRD pattern after the measured intensity is corrected for polarization, reabsorption and inelastic scattering and converted to electron units using the mean square scattering factor $\langle f^2 \rangle$ [32]. An evaluation of the background contribution to the normalized XRD pattern and its subtraction yields the contribution of nanometric crystallites. The background was estimated using the OriginLab software [26]. Due to the fact that the contribution of the interfacial component to the XRD pattern is diffuse, its evaluation and interpretation require care. This approach was applied in this study to the AlSb compound obtained after 10 h of milling because this sample has the largest amount of AlSb; the estimated volume fractions of the crystalline and interfacial components were ≈68% and 32%, respectively.

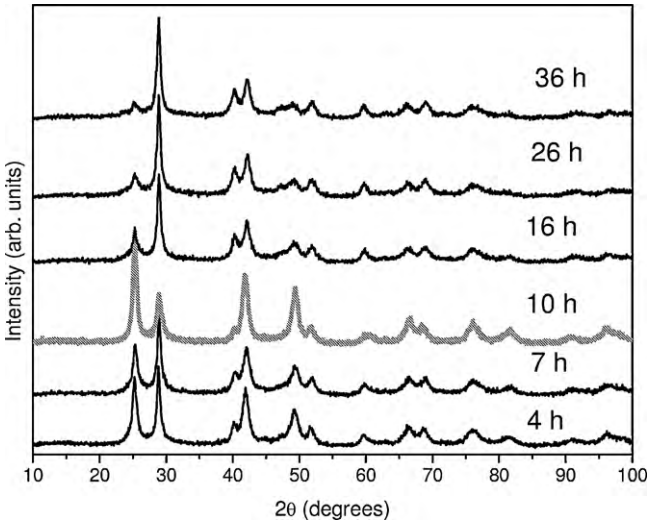

Fig. 1. XRD patterns of an AlSb mixture for several milling times.

All XRD patterns were simulated using the Rietveld structural refinement procedure [33] and the DBWS-9807 code. For this, the structural models given in the ICSD codes above were used. The best simulation of the XRD pattern for 10 h of milling was achieved assuming a lattice parameter $a = 0.61151$ nm, which is slightly smaller than that given in Ref. [17]. The experimental and simulated XRD patterns are shown in Fig. 2, where one can see an excellent agreement between the experimental and simulated patterns. The relative amounts of the phases were also obtained from the Rietveld analysis and the values for AlSb and elemental Sb were 73 (50)% and 27 (18)%, respectively. The numbers between parentheses are the relative amounts of the phases taking into account the estimated volume fraction of the interfacial component.

When the cell volume of AlSb is plotted as a function of milling time, one can see a minimum at about 7 h of milling as shown in Fig. 3. According to Fig. 1, the maximum volume fraction of AlSb is reached for about 10 h of milling. Thus, one can conclude that between 7 and 10 h of milling the maximum volume fraction of AlSb phase is obtained and that there is a lattice expansion of the AlSb for times larger than 7 h that promotes its dissociation.

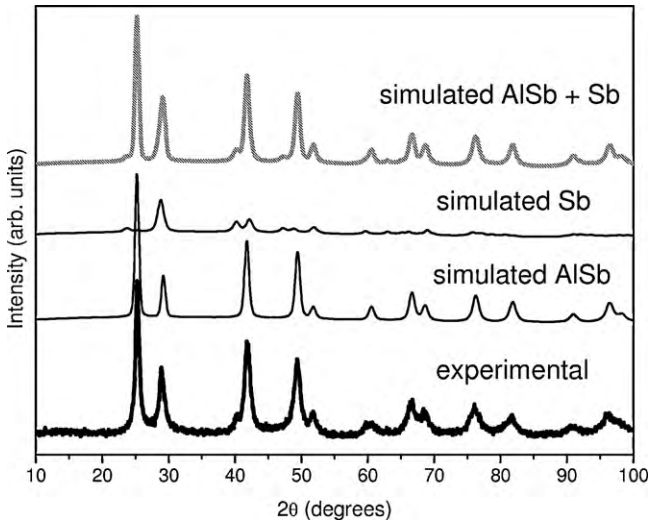

Fig. 2. Measured and simulated XRD patterns of a sample milled for 10 h.

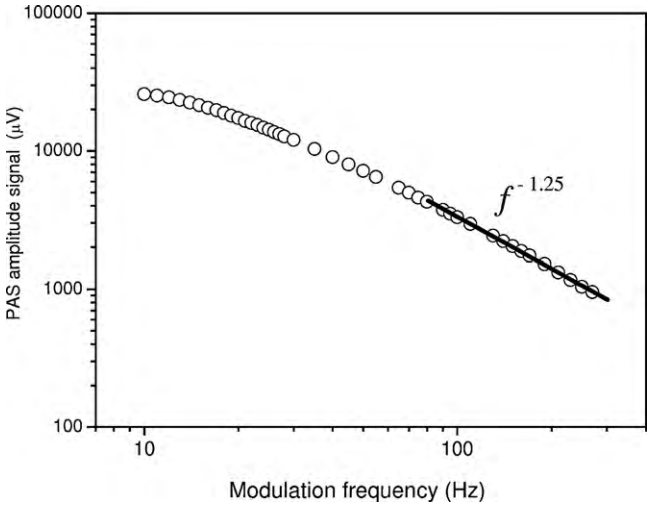

Fig. 4. PAS signal amplitude versus modulation frequency for a sample milled for 10 h.

All peaks of the XRD pattern for 10 h of milling shown in Fig. 1 are broadened, indicating a nanometric AlSb phase. The mean size of the crystallites can be estimated from the simulated XRD pattern taking into account the line broadening caused by both crystallite size and strain through the equation [34]

$$\left(\frac{\beta_t \cos\theta}{K\lambda}\right)^2 = \frac{1}{d^2} + \sigma_p^2\left(\frac{\sin\theta}{K\lambda}\right)^2, \quad (5)$$

where θ is the diffraction angle, λ is the X-ray wavelength, β_t is the total peak broadening measured at the full-width at half-maximum (FWHM) in radians, d is the crystallite size, σ_p is the strain, and K is a constant which depends on the measurement conditions and on the definitions of β_t and d. Here, K was taken as 0.91 as is generally the case in the Scherrer formula. Graphical linearization of the above relationship, i.e., plotting $\beta_t^2 \cos^2\theta/\lambda^2$ versus $\sin^2\theta/\lambda^2$, yields the mean crystallite size free from strain effects from the values of the intercept of the straight line, as well as the strain from the slope. The DBWS 9807 code generates the β_t and 2θ positions for all simulated peaks. Considering these values in Eq. (5), the values found were $d \approx 33$ nm and $\sigma_p \approx 1.7\%$. These results confirm the nanometric form of AlSb.

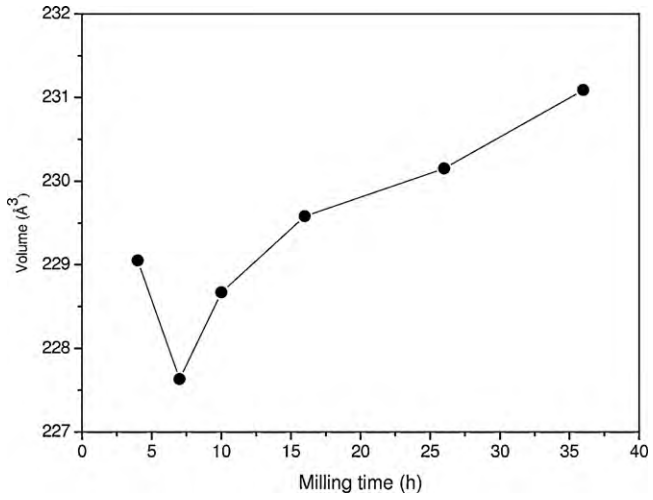

Fig. 3. Volume fraction of the AlSb phase as a function of milling time. The solid line is a guide to the eye.

4.2. PAS measurements

The characteristic frequency $f_c = \alpha/\pi l^2$ is the modulation frequency for the transition from the thermally thin regime ($f < f_c$) to the thermally thick regime ($f > f_c$). In this expression, α is the thermal diffusivity and l is the sample thickness. Since the thermal diffusivities of AlSb phase was not found in the literature, the value was estimated using the equation $K = \rho C_p \alpha$, where K is the thermal conductivity, ρ is the density, C_p is the specific heat, and α is the thermal diffusivity. The TAPP software [17] gives the values of $\rho = 4276$ kg/m^3 and $C_p = 333$ J/kg K for AlSb and $\rho = 6741$ kg/m^3 and $C_p = 207$ J/kg K for elemental Sb. Borca-Tasciuc et al. [35] reported a value of 57 W/mK for the thermal conductivity of bulk AlSb, while the PTOE software [36] gives a value of 24.3 W/mK for elemental Sb. These values were used in the equation above to calculate the thermal diffusivity and the results were $\alpha = 0.40 \times 10^{-4}$ m^2/s for bulk AlSb and 0.17×10^{-4} m^2/s for elemental Sb. These values were used to calculate the characteristic frequency f_c. In this study only the sample milled for 10 h was investigated by PAS because it has the largest volume fraction of AlSb. Since its thickness is 450 μm, a characteristic frequency of 62 Hz was calculated. The PAS data were acquired between 10 and 270 Hz in order to achieve a thermally thick regime.

Figs. 4 and 5 show the PAS signal amplitude and phase for the sample milled for 10 h. The procedure described in Section 2 to find the contribution of each process to PAS signal amplitude was applied. From Fig. 4, one can see that between 70 and 270 Hz, the PAS signal amplitude changes with modulation frequency as $f^{-1.25}$, which is near $f^{-1.0}$, characteristic of nonradiative surface recombination, thermoelastic bending, or thermal dilation [37]. Thermal dilation produces a signal whose phase is independent of the modulation frequency and equal to −90°. As shown in Fig. 4, this behavior is not observed, allowing us to disregard this heat transfer mechanism. The absence of thermoelastic bending was verified by it not being possible to fit the phase data to the Eq. (4). On the other hand, the expression for the phase corresponding to the nonradiative surface recombination mechanism, reproduced as Eq. (3), was fitted to the Φ_{ph} (radians) versus f plot in the modulation frequency range of 90–270 Hz. The observed deviation of frequency dependence of the PAS signal from the theoretical expectation $f^{-1.0}$ to $f^{-1.25}$ can be associated with a partial overlap of nonradiative bulk and surface recombination mechanisms because both processes have the same expression for the signal phases.

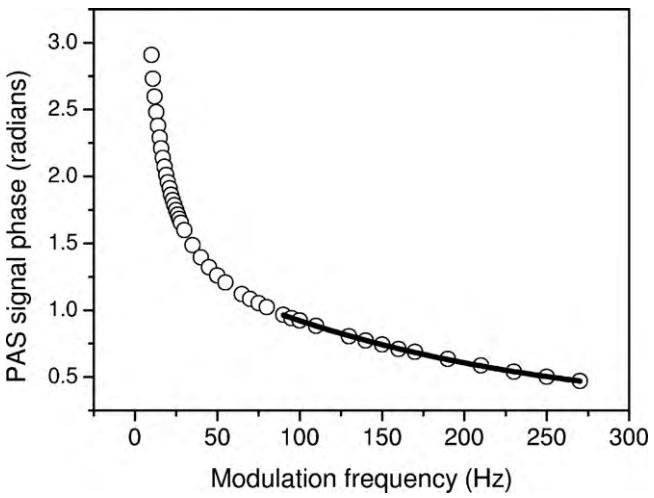

Fig. 5. PAS signal phase versus modulation frequency for a sample milled for 10 h. The solid line corresponds to the best fit of experimental data to Eq. (3).

In order to fit the theoretical result to the experimental curve, we estimated an initial value for α assuming that the thermal diffusivity of sample could be described as a random binary mixture of the phases present in the sample. Landauerĭs paper [38] reports an expression that describes quite well the electrical properties of binary metallic mixtures. Since electrons drive heat and the electricity (see Wiedemann–Franz law), this expression has also been used in this study to evaluate the thermal properties (thermal diffusivity and thermal conductivity) of a random binary mixture of AlSb and elemental Sb, and is written as

$$\alpha_{\text{mixture}} = \frac{1}{4}\left\{(3x_2-1)\alpha_2+(3x_1-1)\alpha_1 + \left[((3x_2-1)\alpha_2+(3x_1-1)\alpha_1)^2+8\alpha_1\alpha_2\right]^{1/2}\right\} \quad (6)$$

where x_i (i = 1,2) is the relative amount of AlSb and elemental Sb phases obtained from the Rietveld analysis and α_1 and α_2 are the thermal diffusivities of bulk AlSb and elemental Sb, respectively. A value of $\alpha_{\text{mixture}} = 0.326 \times 10^{-4}\ \text{m}^2/\text{s}$ was obtained. Bennett et al. [10] reported values for the mobility of the excess carriers at room temperature between 61 and $300 \times 10^{-4}\ \text{m}^2/\text{s}$. Under these conditions, the best fit was reached considering the following values: $\alpha_{\text{sample}} = 0.321 \times 10^{-4}\ \text{m}^2/\text{s}$, $D = 62.6 \times 10^{-4}\ \text{m}^2/\text{s}$, $\nu = 205 \times 10^{-2}\ \text{m/s}$ and $\tau = 0.41\ \mu\text{s}$. The fit is shown in Fig. 5. The good agreement of the thermal diffusivity values corroborates our assumption.

Based on the previous expression (6), it is interesting to compare the thermal conductivity reported in Ref. [35] with the one calculated for a random binary mixture of the phases present in the sample, using the expression [38].

$$K_{\text{mixture}} = \frac{\alpha_{\text{meas}}}{4}\left\{(3x_2-1)A+(3x_1-1)B + \left[((3x_2-1)A+(3x_1-1)B)^2+8AB\right]^{1/2}\right\}$$

$$A = (\rho C_p)_{\text{Sb}} \text{ and } B = (\rho C_p)_{\text{AlSb}}, \quad (7)$$

where ρ is density obtained from the Rietveld analysis, C_p is the specific heat listed above, and x_i (i = 1,2) are AlSb and elemental Sb concentrations, respectively. The term between brackets is the volumetric heat capacity of a random binary mixture. Considering the values of $\rho = 4320\ \text{kg/m}^3$ and $6757\ \text{kg/m}^3$ for as-milled AlSb and Sb, respectively, and the values of C_p given in Ref. [17], a value of 46 W/mK is obtained. This value is ≈19% smaller than that reported in Ref. [35]. This result seems to corroborate the suggestion, found in the literature, that the thermal conductivity can be smaller in materials having nanometric crystallites [39].

In a previous study [40], we measured the thermal diffusivity of nanostructured single phase ZnSe produced by MA. The value for as-milled ZnSe was 51% larger than after annealing, which was similar to the value of bulk ZnSe ($\alpha = 0.101 \times 10^{-4}\ \text{m}^2/\text{s}$). Based on these results, it is interesting to estimate the contribution of the interfacial component to thermal diffusivity value. For this, we will assume that the measured thermal diffusivity is equal to the weighted sum of thermal diffusivity of the crystalline and interfacial components and elemental Sb. Thermal diffusivity values of bulk AlSb and elemental Sb and the volume fractions obtained by taking into account the interfacial component will be considered. The weighted value of the thermal diffusivity is written as

$$\alpha_{\text{sample}} = x\alpha_{\text{AlSb}} + y\alpha_{\text{int}} + z\alpha_{\text{Sb}} \quad (8)$$

where $x = 0.50$, $y = 0.32$, $z = 0.18$, $\alpha_{\text{AlSb}} = 0.40 \times 10^{-4}\ \text{m}^2/\text{s}$, and $\alpha_{\text{Sb}} = 0.17 \times 10^{-4}\ \text{m}^2/\text{s}$. Using these values in Eq. (8) a value of $\alpha_{\text{int}} = 0.282 \times 10^{-4}\ \text{m}^2/\text{s}$ is calculated. This value represents ≈88% of the obtained from the PAS data. This result shows that for milled materials having a large interfacial component, the contribution of this component to thermal diffusivity of sample is very significant. Annealing the sample can significantly reduce this contribution, as it was shown in Ref. [40].

5. Conclusions

Several conclusions are obtained from this study. The main ones are the following:

Milling mixture of Al and Sb with nominal AlSb composition, leads the formation of nanostructured AlSb and elemental Sb.
The maximum volume fraction of AlSb is obtained for milling times between 7 and 10 h.
For milling times larger than 10 h, the AlSb phase starts to dissociate, leading to an increase in elemental Sb.
The volume fractions of the crystalline and interfacial components were evaluated through an approach in which the XRD pattern is converted to electron units by using the mean square scattering factor $\langle f^2 \rangle$. Its combination with the Rietveld structural refinement procedure is used to evaluate the volume fractions of AlSb and elemental Sb.
The thermal diffusivity and other heat transport parameters for nanostructured AlSb were obtained from the PAS amplitude and phase.
Thermal behavior (thermal diffusivity and thermal conductivity) of AlSb after 10 h of milling is similar to that of a random binary mixture of the AlSb and elemental Sb.
The contribution of the interfacial component to the thermal diffusivity of milled materials can be very significant. Annealing the sample can reduce this contribution.

Acknowledgments

The authors thank Conselho Nacional de Desenvolvimento Científico e Tecnológico (CNPq), FINEP, CAPES, and FAPESC, Brazil, for financial support.

References

[1] H. Gotoh, K. Sasamoto, S. Kuroda, M. Kimata, Phys. Status Solidi A 75 (1983) 641.
[2] C. An Chang, H. Takaoka, L.L. Chang, L. Esaki, Appl. Phys. Lett. 40 (1982) 983.

[3] J.H. Yee, S.P. Swierkowski, J.W. Sherohman, IEEE Trans. Nucl. Sci. NS-24 (1977) 1962.
[4] X.-C Cheng, T.C. McGill, J. Vac. Sci. Technol. B 16 (4) (1998) 2291.
[5] J.B. Boos, W. Kruppa, B.R. Bennett, D. Park, S.W. Kirchoefer, R. Bass, H.B. Dietrich, IEEE Trans. Electron. Devices 45 (1998) 1869.
[6] J.B. Boos, M.J. Yang, B.R. Bennett, D. Park, W. Kruppa, C.H. Yang, R. Bass, Electron. Lett. 34 (1998) 1525.
[7] M. Johnson, B.R. Bennett, M.J. Yang, M.M. Miller, B.V. Shanabrook, Appl. Phys. Lett. 71 (1997) 974.
[8] M.D. McCluskey, E.E. Haller, P. Becla, Phys. Rev. B 65 (2001) 045201.
[9] O. Mann, C.L. Aravinda, W. Freyland, J. Phys. Chem. B 110 (2006) 21521.
[10] B.R. Bennett, W.J. Moore, M.J. Yang, B.V. Shanabrook, J. Appl. Phys. 87 (2000) 7876.
[11] C. Suryanarayana, Prog. Mater. Sci. 46 (2001) 1.
[12] M. Nogami, K. Nagaska, E. Kato, J. Am. Ceram. Soc. 73 (1990) 2097.
[13] J.D. Stucky, J.E. Macdougall, Science 247 (1990) 669.
[14] J. Che, X. Yao, H. Jian, M. Wang, Ceram. Int. 30 (2004) 1935.
[15] H. Gleiter, Nanostruct. Mater. 1 (1992) 1.
[16] E.A. Stern, R.W. Siegel, M. Newville, P.G. Sanders, D. Haskel, Phys. Rev. Lett. 75 (1995) 3874.
[17] TAPP software, Version 2.2, Wade Court, Hamilton, OH, E.S. Microwave Inc.
[18] H. Honda, H. Sakaguchi, Y. Fukuda, T. Esaka, Mater. Res. Bull. 38 (2003) 647.
[19] C.-M. Park, H.-J. Sohn, Chem. Mater. 20 (2008) 3169.
[20] G. Ziegler, D.P.H. Hasselman, J. Mater. Sci. 16 (1981) 495.
[21] A. Rosencwaig, A. Gersho, J. Appl. Phys. 47 (1976) 64.
[22] A. Nozik, Annu. Rev. Phys. Chem. 52 (2001) 193.
[23] G. González de la Cruz, Y.G. Gurevich, J. Appl. Phys. 80 (1996) 1726.
[24] G. González de la Cruz, Y.G. Gurevich, Phys. Rev. B 58 (1998) 7768.
[25] A. Pinto Neto, H. Vargas, N.F. Leite, L.C.M. Miranda, Phys. Rev. B 41 (1990) 9971.
[26] Microcal Origin version 6, Microcal Software, Inc., One Roundhouse Plaza, Northampton, MA 01060, USA.
[27] J.C. deLima, N. Cella, L.C.M. Miranda, C. Chying An, A.H. Franzan, N.F. Leite, Phys. Rev. B 46 (1992) 14186.
[28] Inorganic Crystal Structure Database (ICSD), Gmelin-Institut für Anorganische Chemie and Fachinformationszentrum FIZ Karlsruhe, 1995.
[29] K. Ersching, C.E.M. Campos, J.C. de Lima, T.A. Grandi, Mater. Chem. Phys. 112 (2008) 745.
[30] J.C. de Lima, M. Schmitt, S.M. Souza, T.O. Almeida, A.R. Jeronimo, D.M. Triches, T.A. Grandi, C.E.M. Campos, J. Alloys Compd. 436 (2007) 13.
[31] C.M. Poffo, J.C. de Lima, S.M. Souza, D.M. Trichês, T.A. Grandi, R.S. de Biasi, Journal of Raman Spectroscopy, submitted for publication, doi:10.1002/jrs.2623.
[32] C.N.J. Wagner, in: S.Z. Beer (Ed.), Liquid Metals, Marcel Dekker, New York, 1972, p. 258.
[33] H.M. Rietveld, J. Appl. Crystallogr. 2 (1969) 65.
[34] Z. Strnad, Glass-Ceramic Materials, Glass Science and Technology, vol. 8, Elsevier, Amsterdam, 1986, pp. 161.
[35] T. Borca-Tasciuc, D. Achimov, W.L. Liu, G. Chen, in: G.P. Celeta (Ed.), Proceedings of the Heat Transfer and Transport Phenomena in Microscale, Banff, Canada, 2000, p. 369.
[36] PTOE software found on the www.chemglobe.org/ptoe.
[37] G. Rousset, L. Lepoutre, L. Bertrand, J. Appl. Phys. 54 (1983) 2383.
[38] R. Landauer, J. Appl. Phys. 23 (1952) 779.
[39] S. Ur, P. Nash, I. Kim, J. Mater. Sci. 38 (2003) 3553.
[40] J. Baltazar-Rodrigues, J.C. de Lima, C.E.M. Campos, T.A. Grandi, J. Phys.: Condens. Matter 20 (2008) 465205.